

Motion of oil in water induced by osmosis in a confined systemErwan Crestel,¹ Anežka Kvasničková,¹ Enric Santanach-Carreras ,²
Jérôme Bibette,¹ and Nicolas Bremond ^{1,*}¹*Laboratoire Colloïdes et Matériaux Divisés, CBI, ESPCI Paris,
Université PSL, CNRS, 75005 Paris, France*²*Total SA, Pôle d'Etudes et Recherche de Lacq, BP 47, 64170 Lacq, France*

(Received 11 May 2020; accepted 10 September 2020; published 2 October 2020)

Gradients of chemical potentials in a multiphase system induce mass transport and thus motion of liquid-liquid interfaces. We probe the displacement of oil on a solid substrate immersed in water through this osmosis phenomenon by using two experimental microfluidic systems. The first one, based on glass capillary, is used to quantify the permeability to water of oils sandwiched between two different salt solutions that set the water flux and thus oil motion dynamics. In the context of oil recovery, in particular in the case of low-salinity water flooding, we show that the presence of asphaltenes increases the flux of water and thus the velocity of oil. The second system involves microfabricated cavities that play the role of dead-end pores where oil is trapped in the presence of a salt crystal. The salt crystal allows nucleation of a water drop inside the microcavities that swells under osmosis, thus moving oil out of the dead-end pore model. The efficiency of oil removing from the model crevice is shown to be a function of geometrical and wetting properties, including heterogeneities of surface features. Counterintuitively, it is less probable for oil to move out from a hydrophilic cavity than from a hydrophobic one. Experimental observations are rationalized by geometrical arguments.

DOI: [10.1103/PhysRevFluids.5.104003](https://doi.org/10.1103/PhysRevFluids.5.104003)**I. INTRODUCTION**

Wetting of oil on solid surfaces in the presence of water results from a complex interplay of molecular interaction forces [1]. In addition, surface roughness and chemical heterogeneities promote pinning of the contact line, leading to contact angle hysteresis and thus increase complexity on the wetting behavior when oil is displaced on solids. Removing oil from a solid substrate immersed in water is usually achieved by adding surface active molecules that modify surface energies and thus wetting properties [2]. In the context of enhanced oil recovery, the injection of low-salinity water into rock reservoirs, namely, low-salinity water flooding, has been shown to potentially favor oil extraction [3,4]. The efficiency of such a process depends on the geological properties of the medium composed of various rock compositions, crude oil, connate water, or fines. There is no clear consensus on the underlying mechanisms at play, but several scenarios have been proposed, most of them involving interfacial properties alteration, due to, for example, ion adsorption [5] or dissolution of rock in carbonate reservoirs [6]. Another mechanism involves osmosis, where oil acts as a semipermeable membrane that separates low- and high-salinity waters, which can lead to oil relocation [7–9]. Indeed, oil initially trapped in dead-end pores of the rock or that has not been removed from the rock during water injection is in contact between low-salinity water and connate water that contains high amount of salts. Then a small but finite solubility of

*Nicolas.Bremond@espci.fr

water in oil allows water transfer from one aqueous phase to the other one, thus inducing oil motion. Such a permeation phenomenon is widely encountered in biphasic systems such as foams and emulsions that alter stability via ripening [10,11] or, in the case of emulsions, can be used to assess microorganism bioenergetics [12] or to induce structural rearrangement of adhesive emulsion [13,14]. The use of microfabrication techniques is well suited for studying such a phenomenon as it allows one to well control geometry and fluid composition, from model emulsion system [15] to model oil reservoirs [16,17].

Here we investigate oil motion induced by osmosis in confined systems and its link to wettability properties with two experimental setups. The first one mimics a single pore where oil is sandwiched between two reservoirs of salted water having different concentrations. This allows us to probe water permeability features of various organic membranes, from pure hydrocarbon to crude oil. Then we take advantage of microfabrication techniques for making microcavities that act as dead-end pores where oil is trapped. The presence of a salt crystal inside the model crevice allows us to attract water from the surroundings and thus to nucleate a water drop inside the microcavities that swells under osmosis. The fate of the oil volume blown by osmosis is experimentally explored for various sizes and aspect ratios of the microcavity, wetting properties, and osmotic pressures.

II. MATERIALS AND METHODS

A. Glass capillary experiments

The water phases are solutions of sodium chloride (Sigma Aldrich) prepared from milli-Q water. The model oil is an alkane, octane (Sigma Aldrich), used as purchased. Crude oil and asphaltenes are furnished by Total SA. The viscosity of the crude oil at 30 °C is 6.7 mPa·s and its density is 825 kg/m³. Asphaltenes are solubilized in toluene (Sigma Aldrich). To measure water content in oil phases, we perform Karl Fischer titrations using an 831 KF Coulometer (Metrohm AG). The titration medium is a mixture of HYDRANAL Coulomat AG-H and toluene at a weight percentage ratio of 80:20. Both chemicals are used as received from the supplier. Prior to the titration, the samples, about 10 ml in volume, are homogenized using a vortex mixer (Heidolph Topmix) for 2 min. Between 0.1 and 0.3 g of this homogenized samples is used for the titration. The solubility of water in octane at 30 °C is (78 ± 1) mg/kg, in crude oil it is equal to (310 ± 5) mg/kg, and in toluene with and without asphaltenes it is (520 ± 8) and (510 ± 8) mg/kg, respectively.

The glass capillaries (Vitrocom) have an outer diameter of 1 mm and an inner one of 0.78 mm. One end of the capillary is first tapered with the help of a gravitational puller (PC-10, Narishige) and then cut using a microforge (M900, Narishige). The final length of the capillary is 5 cm. Their surface is silanized with chlorotrimethylsilane (Sigma Aldrich) to create a homogeneous wetting condition. As sketched in Fig. 1, the procedure for preparing an oil meniscus sandwiched between two salted solutions relies on capillary imbibition. Since water still wets the silanized glass surface, the capillary is first completely filled with low-salinity water (LSW) by plunging the tapered end in a water contained in a syringe (Fig. 1, steps 1 and 2). The oil is then introduced from the tapered end also by using capillary force but with the help of a wipe at the opposite extremity (Fig. 1, step 3). The liquid motion is thus driven by the capillary pressure set by the wipe mesh size. The volume of oil sucked into the capillary can be controlled by varying the contact time between the wipe and the tube extremity. The high-salinity water (HSW) is finally pumped in the capillary, also with a wipe, until the oil meniscus is placed at the tube center (Fig. 1, step 4). Given the inner tube diameter and the wetting conditions, the minimal meniscus length is about 200 μ m. To make a dead-end pore, the tapered end is stuck into a piece of a gas-tight septum made of butylene elastomer (Bellco) (Fig. 1, step 5) and immersed in LSW (Fig. 1, step 6). Up to seven glass capillaries are fixed at the bottom wall of a sealed glass box which is filled with LSW. The sealing is realized with a glue that requires about 10 h to harden. The motion of the oil menisci is thus monitored the day after their formation. The glass box is finally placed in a case that fits on an XY motorized stage (MAX202, Thorlabs) mounted on a microscope (DMI 3000, Leica) and where water, from a temperature regulated water

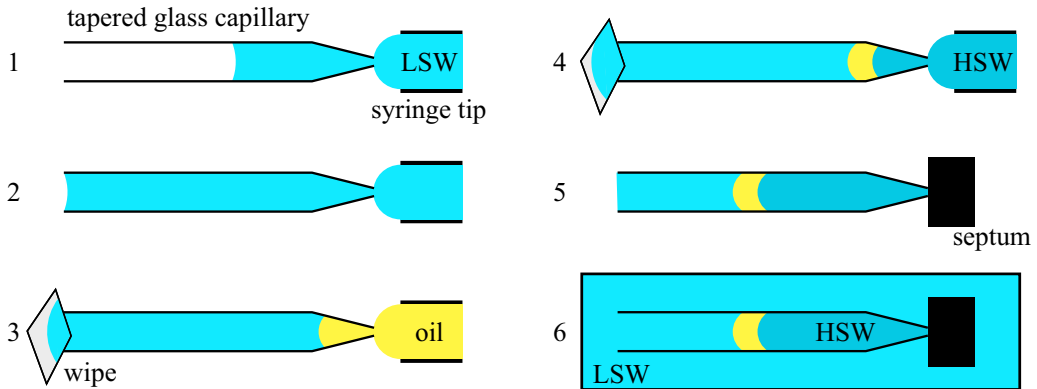


FIG. 1. Procedure based on capillary imbibition for preparing an oil meniscus trapped in a glass capillary between two salt solutions.

bath, can flow through. The thermal connection with the box containing the glass capillaries is realized with the help of paraffin oil. The whole microscope is finally enclosed in a box to avoid thermal convection with the surrounding environment. In that way, the temperature fluctuations over 12 days are less than $0.25\text{ }^{\circ}\text{C}$. Experiments are performed between $30\text{ }^{\circ}\text{C}$ and $50\text{ }^{\circ}\text{C}$.

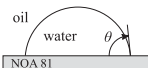
Snapshots of oil menisci are acquired with a CCD camera (GO 5000, Jai) every 30 min. They are then analyzed with dedicated image processing programs developed with MATLAB. In that way, oil meniscus features, such as center of mass and radii of curvature, are evaluated as a function of time.

B. Microcavity experiments

The water phase is an aqueous solution of sodium chloride (Sigma Aldrich) prepared from milli-Q water at a concentration C_s . The model oil is an alkane, hexadecane (Sigma Aldrich), used as purchased. Microcavities are made in a thin layer of a thiolene-based resin NOA81 (Norland optical adhesive) by a stamping method [18]. Polydimethylsiloxane (PDMS) stamps, composed of arrays of cylindrical rods having various diameters and heights, are fabricated by standard soft lithography methods [19]. The pattern is transferred on a thin layer of NOA81 that is deposited on a glass coverslip by a spin coating step. The PDMS stamp is pressed onto the resin layer and irradiated with UV (LC8, Hamamatsu) for 80 s. Then the glass coverslip is bounded on a glass slide which is finally bounded to a plastic Petri dish. The contact angle between the aqueous phase, oil, and the resin surface is measured with a drop shape analyzer (DSA30, Krüss). NOA81 is naturally hydrophobic but its surface energy can be modified when exposed to oxygen plasma. The surface becomes more and more hydrophilic when increasing the exposure time of oxygen plasma (Femto, Diener Electronic) set at 70% of its maximal power and for an ambient air pressure of $4 \times 10^4\text{ Pa}$ for 6 and 12 s or $2 \times 10^4\text{ Pa}$ for 30 s. The advancing and receding contact angles are reported in Table I.

Microcavities are used for trapping water and oil successively, like air for the investigation of heterogeneous nucleation of bubbles under low pressure [20]. The different steps for preparing microcavities before experiments are sketched in Fig. 2. First, the HSW is put under vacuum (Laboport, KNF) to remove part of the dissolved gases, set at $1 \times 10^4\text{ Pa}$ for 10 min under stirring. Then $800\text{ }\mu\text{l}$ are dropped on the patterned substrate in the Petri dish (Fig. 2, step 1). Using degassed water allows for the water to enter the hydrophobic microcavities. Indeed, since experiments are done at atmospheric condition, the water is unsaturated and gas molecules thus diffuse from air pockets, initially trapped in microcavities due to contact line pinning at cavity edge during the immersion step, towards the surrounding water in order to balance their chemical potential. Once

TABLE I. Advancing and receding contact angles between aqueous solutions and oil on bare and plasma-treated solid substrates made of NOA81.

Water		Bare surface	Plasma, 6 s	Plasma, 12 s	Plasma, 30 s
LSW	θ_a (deg)	147 ± 7	130 ± 1	96 ± 3	67 ± 3
	θ_r (deg)	83 ± 2	64 ± 4	50 ± 2	16 ± 1
HSW	θ_a (deg)	126 ± 2		80 ± 4	
	θ_r (deg)	85 ± 4		46 ± 5	

microcavities are filled with water, the water excess is removed with a pipette, leaving water only in the microcavities (Fig. 2, step 2). The Petri dish is placed at 65°C for 15 min in an oven to evaporate the trapped water, leaving a salt crystal in each microcavity (Fig. 2, step 3). Then $150\ \mu\text{l}$ of degassed hexadecane is deposited onto the array of microcavities (Fig. 2, step 4). After complete impregnation, the excess of oil is sucked out by a tissue, leaving only oil in the microcavities (Fig. 2, step 5). The substrate is finally immersed in a large amount of LSW, corresponding to water depth in the Petri dish of about 5 mm (Fig. 2, step 6). Efficient oil trapping is not possible for the most hydrophilic case and osmosis experiments cannot be performed for such wetting conditions.

The motion of oil is monitored with a high-speed camera (Fastcam Mini UX100, Photron) mounted on a inverted microscope (DMI-3000, Leica) through a $10\times$ or $40\times$ objective. Experiments are realized at room temperature, between 21°C and 23°C . Features of the oil motion are averaged from about 60 microcavities for an experiment and from up to three repeated experiments.

III. RESULTS AND DISCUSSION

A. Moving oil in a capillary

An example of an oil meniscus trapped in a glass capillary and surrounded by two aqueous phases having different salt concentrations is shown in Fig. 3(a). Here the shape of the meniscus adopts a cylindrical symmetry. The center of mass of the meniscus thus lies at the center of the capillary and its longitudinal location is denoted by z_c . The time evolution of z_c is reported in Fig. 3(b). The

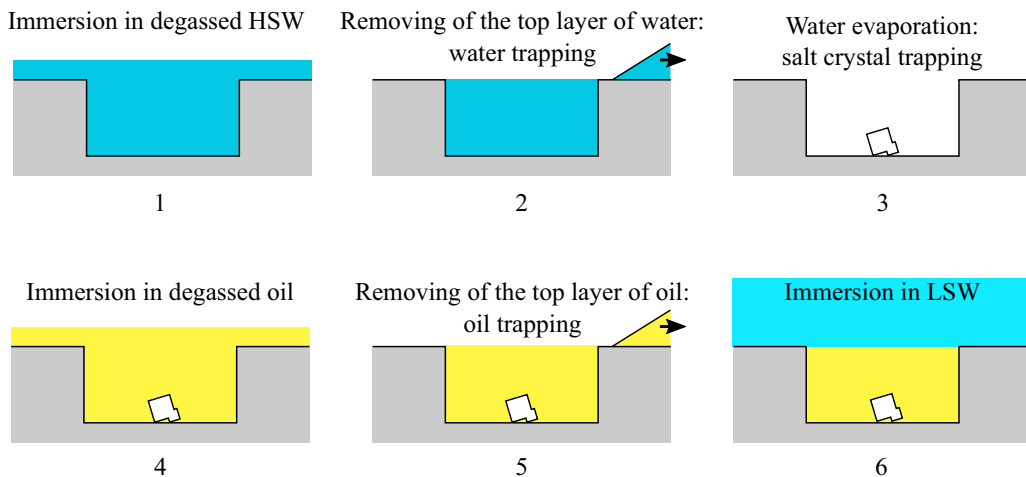


FIG. 2. Schematics of the different steps for preparing microcavity experiments.

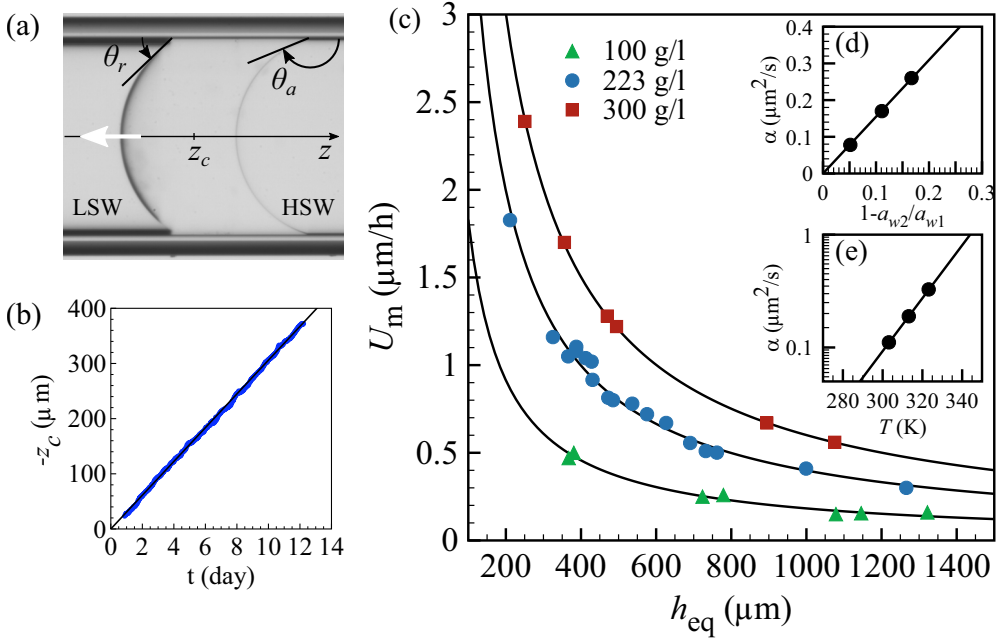


FIG. 3. (a) Snapshot of an oil meniscus (octane) sandwiched between two salted solutions (LSW and HSW) in a glass capillary. The arrow indicates the direction of oil displacement. Advancing and receding contact angles are also indicated. The inner capillary diameter is 0.78 mm. (b) Time evolution of the center of mass of oil. (c) Evolution of the meniscus velocity U_m as a function of the equivalent oil meniscus thickness h_{eq} given by Eq. (12) for different salt concentrations C_{HSW} . The solid line is a fit by Eq. (10), i.e., $U_m = \alpha/h_{eq}$. The temperature T is 30°C. (d) Coefficient α as a function of the relative mismatch of water activity. (e) Coefficient α as a function of temperature for $C_{HSW} = 223$ g/l. The solid line is an exponential fit (see the text for details).

oil is moving from right to left since the water is diffusing through the oil from low to high salt concentrations. This motion is observed to be linear with time. We notice small fluctuations of z_c that are correlated to slight irregular motion of the contact lines undergoing pinning and depinning events that are not synchronized all along the meniscus periphery. This behavior is more pronounced for a bare glass surface and the surface treatment helps to get more homogeneous wetting conditions while contact angle hysteresis cannot be avoided. We also mention that temperature is another key parameter to control for monitoring such a thermally activated phenomenon over a few days. Because of that control, one can confidently estimate a velocity of the meniscus U_m from the curve $z_c(t)$. This velocity is reported in Fig. 3(c) as a function of an equivalent meniscus length h_{eq} for various concentrations of the HSW. As discussed below, h_{eq} corresponds to the thickness of an oil slug having flat interfaces while giving rise to the same water flux as the corresponding curved meniscus. The meniscus velocity is inversely proportional to its length, i.e., $U_m = \alpha/h_{eq}$. This is reminiscent of solvent flux through a semipermeable membrane [21]. Let us determine the expression of α in the present configuration.

We first consider two aqueous solutions in a capillary tube of radius r_c and separated by a meniscus of oil having a length h [Fig. 4(a)]; the interfaces are flat. Both aqueous reservoirs contain a solute at mole fractions $x_{s,1}$ and $x_{s,2}$, respectively. Since water is slightly soluble in the oil phase, the chemical potential of water in oil $\mu_{w,o}$ can be considered as the one of an ideal solution. In that case, it is written

$$\mu_{w,o}(z) = \mu_w^0 + \mathcal{R}T \ln x_{w,o}(z), \quad (1)$$

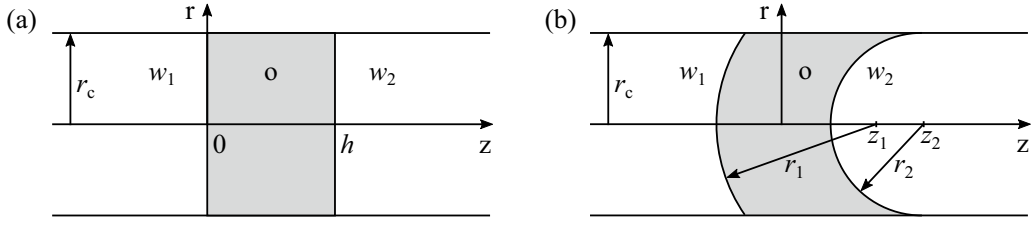


FIG. 4. Schematics of two aqueous phases (w_1 and w_2) in a round capillary separated by an oil meniscus with (a) flat and (b) curved interfaces.

where $x_{w,o}$ is the concentration of water at a location z , μ_w^0 is the chemical potential of pure water that depends on the pressure and temperature, and \mathcal{R} is the gas constant. At equilibrium, the equality of the chemical potentials of water at each interface gives

$$\mu_{w1} = \mu_w^0 + \mathcal{R}T \ln x_{w,o}(0), \quad (2)$$

$$\mu_{w2} = \mu_w^0 + \mathcal{R}T \ln x_{w,o}(h), \quad (3)$$

where μ_{w1} and μ_{w2} are the chemical potentials of water in reservoirs 1 and 2, respectively. The concentrations of water in oil below both interfaces are thus linked as

$$x_{w,o}(h) = x_{w,o}(0) e^{\Delta\mu_w/\mathcal{R}T}, \quad (4)$$

with $\Delta\mu_w = \mu_{w2} - \mu_{w1}$. For a stationary regime, the flux of water J_w through the oil meniscus driven by the concentration gradient is

$$J_w = -D_w \frac{dc_{w,o}}{dz} = -D_w c_{w,o}(0) \frac{e^{\Delta\mu_w/\mathcal{R}T} - 1}{h}, \quad (5)$$

where D_w is the coefficient of diffusion of water molecules in oil. The concentration of water in oil $c_{w,o}$ is linked to the molar fraction $x_{w,o}$ and the molar volume of oil v_o , i.e., $c_{w,o} = x_{w,o}/v_o$ for an ideal solution.

For the HSW, one has to consider a real solution. In that case, the chemical potential of water containing solutes is

$$\mu_w = \mu_w^0 + \mathcal{R}T \ln(\gamma_w x_w), \quad (6)$$

where γ_w is the activity coefficient of water; γ_w as a function of NaCl concentration is extrapolated from a semiempirical model for monovalent electrolytes [22]. By defining $a_{wi} = \gamma_w x_{wi}$, the water activity in reservoir i , the chemical potential in both aqueous solutions, is

$$\mu_{wi} = \mu_w^0 + \mathcal{R}T \ln(a_{wi}). \quad (7)$$

We note that the interfacial tension γ is not taken into account in the expression of the chemical potential of water since the radius of curvature of the interface is large. In other words, the capillary pressure, of the order of $2\gamma/r_c \simeq 2 \times 10^2$ Pa, where γ is equal to 40 mN/m, is smaller than the osmotic pressure, of the order of $\mathcal{R}T x_s/v_w \simeq 5 \times 10^3$ Pa for the LSW and $-(\mathcal{R}T/v_w) \ln(a_w) \simeq 4 \times 10^7$ Pa for the HSW.

The water flux is finally given by

$$J_w = \frac{S_w D_w}{h} \left(1 - \frac{a_{w2}}{a_{w1}}\right), \quad (8)$$

where $S_w = c_{w,o}(0)$ is the water solubility in oil equilibrated with the least concentrated solution expressed in moles per unit volume. The corresponding volume flow rate Q of water through an

axisymmetric oil meniscus is then

$$Q = 2\pi \int_0^{r_c} J_w v_w r dr, \quad (9)$$

where v_m is the molar volume of water. For flat interfaces, the corresponding velocity of the meniscus $U_m = Q/\pi r_c^2$ is then

$$U_m = \frac{S_w D_w v_w}{h} \left(1 - \frac{a_{w2}}{a_{w1}}\right) = \frac{\alpha}{h}. \quad (10)$$

In the derivation of the water flux, and thus oil velocity, we assume that the water activity in both reservoirs is not affected by mass transfer. Indeed, the length of the HSW plug is about 2.5 cm while the oil moves a few hundred micrometers; the dilution of the NaCl solution is thus around 1% after a few days [Fig. 3(b)].

If the interfaces are curved, as sketched in Fig. 4(b), the oil meniscus thickness h is now a function of the radial location r , and thus the water flux J_w . Knowing the centers of curvature $z_{c,1}$ and $z_{c,2}$ as well as the radii of curvature R_1 and R_2 of both interfaces, one can define an equivalent oil meniscus thickness h_{eq} giving rise to the same flow rate, i.e.,

$$Q = -2\pi \int_0^{r_c} \frac{\alpha}{h(r)} r dr = \pi r_c^2 \frac{\alpha}{h_{eq}}. \quad (11)$$

The equivalent oil meniscus thickness h_{eq} is finally

$$\frac{1}{h_{eq}} = \frac{2}{r_c^2} \int_0^{r_c} \frac{r}{(R_1^2 - r^2)^{1/2} + z_{c,1} - (R_2^2 - r^2)^{1/2} - z_{c,2}} dr. \quad (12)$$

The geometrical features are evaluated for each oil meniscus in order to deduce h_{eq} . As shown in Fig. 3(c), the velocity decrease as a function of h_{eq} is well accounted for by the model. In addition, we note that the evolution of the coefficient α is indeed a linear function of the relative water activity mismatch [Fig. 3(d)]. Finally, we note that for a given composition of the aqueous phases, α increases exponentially with the temperature [Fig. 3(e)]. We indeed find that α ($\mu\text{m}^2/\text{s}$) = $8.55 \times 10^{-9} \exp[5.4 \times 10^{-2} T$ (K)]. Knowing the molar volume of water, the present experiment gives access to an evaluation of the product of the water solubility in oil S_w , in equilibrium with the less salted solution, by the coefficient of diffusion D_w of water molecules in oil. For octane and pure water at 30 °C, $S_w D_w$ is equal to $(3.62 \pm 0.20) \times 10^{-8}$ mol/(m s). When using a higher amount of salt for the LSW, equal to 35 g/l, we estimate a lower value of $S_w D_w$ equal to $(3.1 \pm 0.15) \times 10^{-8}$ mol/(m s), in agreement with a lower solubility of water in oil. While the solubility of water in various solvents is well documented, like water in alkanes, for example [23], the coefficient of diffusion is not, probably because of the lack of a standardized and accessible method. An interesting approach relies on the dissolution rate into a solvent of a water drop held with a micropipette [24]. The authors measured a coefficient of diffusion of water molecules in octane equal to $(5.4 \pm 0.4) \times 10^{-9}$ m²/s at 22 °C. By extrapolating the coefficient α at 22 °C, we estimate a coefficient of diffusion of $(7.4 \pm 0.4) \times 10^{-9}$ m²/s.

The present experimental setup then allows us to evaluate the water permeability of various organic compounds, from pure liquids to complex ones such as light crude oils. For crude oil, we measure a coefficient α equal to $(1.12 \pm 0.06) \times 10^{-13}$ m²/s at 30 °C for $C_{\text{HSW}} = 223$ g/l, which corresponds to $S_w D_w = (3.7 \pm 0.2) \times 10^{-8}$ mol/(m s). The solubility of water in crude oil is 14.9 mol/m³, resulting in a coefficient of diffusion equal to $(2.48 \pm 0.15) \times 10^{-9}$ m²/s. When a solute is smaller than the solvent, the coefficient of diffusion varies with the solvent viscosity η like $1/\eta^p$, where p has been found to be 0.78 for alkanes [24]. However, the value of D_w measured for crude oil is rather large since the viscosity of crude oil is 6.7 mPa s as compared to octane having a viscosity of 0.48 mPa s [25] and for which D_w is estimated to be 1.2×10^{-8} m²/s at

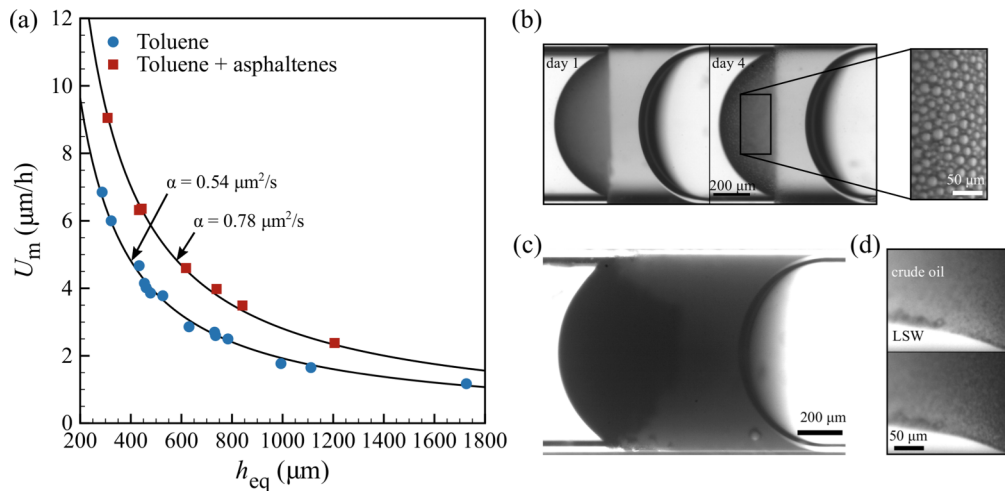


FIG. 5. (a) Velocity of a meniscus made of toluene with and without asphaltenes ($T = 30^\circ\text{C}$, $C_{\text{LSW}} = 0.058\text{ g/l}$, and $C_{\text{HSW}} = 223\text{ g/l}$). (b) Spontaneous emulsification at the interface of LSW and toluene containing asphaltenes. (c) Crude oil meniscus at day 8. (d) Snapshots showing the nucleation of aggregates or droplets at the LSW–crude oil interface at day 1; the time step is 5 h.

30°C , i.e., an increase by a factor 5 to be compared to a decrease of the viscosity by a factor 14 ($14^{0.78} \simeq 7.8$). In order to further investigate this unexpected diffusion feature, we then assess the effect of asphaltenes on the flux of water. Asphaltenes are a compound present in crude oil and mainly composed of polyaromatic carbon rings that are known to have surface activity [26]. Here they are dispersed in toluene at a weight fraction of 0.1%. First, for pure toluene, the coefficient α is equal to $(0.54 \pm 0.02)\ \mu\text{m}^2/\text{s}$ at $T = 30^\circ\text{C}$ [Fig. 5(a)]. This leads to a coefficient of diffusion of water in toluene D_w equal to $(6.8 \pm 0.3) \times 10^{-9}\ \text{m}^2/\text{s}$, close to a previously reported value of $(6.19 \pm 0.5) \times 10^{-9}\ \text{m}^2/\text{s}$ measured at 25°C [27]. While the solubility of water in toluene in the presence of asphaltenes is barely affected at a concentration of 0.1 wt. % [28], there is a relative increase of α , and thus D_w , nearly equal to 50% [Fig. 5(a)]. We also notice the nucleation of water droplets at the interface between toluene and the LSW [Fig. 5(b)], as also recently reported [29]. Since the crude oil is more turbid, it is difficult to clearly distinguish the interface, but a darker region is also observed at the crude oil–LSW interface [Fig. 5(c)]. Also, we notice the apparition of dark spots with time [Fig. 5(d)] that might indicate the presence of droplets. We do not know if these observations are linked to the increase of the water flux, but further investigations are required to decipher the origin of such augmentation.

B. Moving out oil from a microcavity

We now wonder what the fate is of an oil pocket set under motion by osmosis in a porous medium, in particular from a dead-end pore. To this end, cylindrical microcavities where oil is trapped in the presence of salt crystal are now used.

1. Hydrophobic microcavity

Experiments with such microcavities on a bare substrate and observed from above are shown in Fig. 6. The origin of time is taken when the LSW is added onto the microtextured substrate. As indicated in Fig. 6(a), one can clearly see the salt crystal at $t = 0$ that is then dissolved in a growing water pocket as illustrated at $t = 5\text{ min}$. Water from the LSW reservoir thus diffuses through the oil and dissolves the salt crystal in $8 \pm 0.6\text{ min}$. Here the salt concentration of the LSW is 0.058 g/l and the concentration C_s initially used to make the salt crystal is 200 g/l . During the growth of

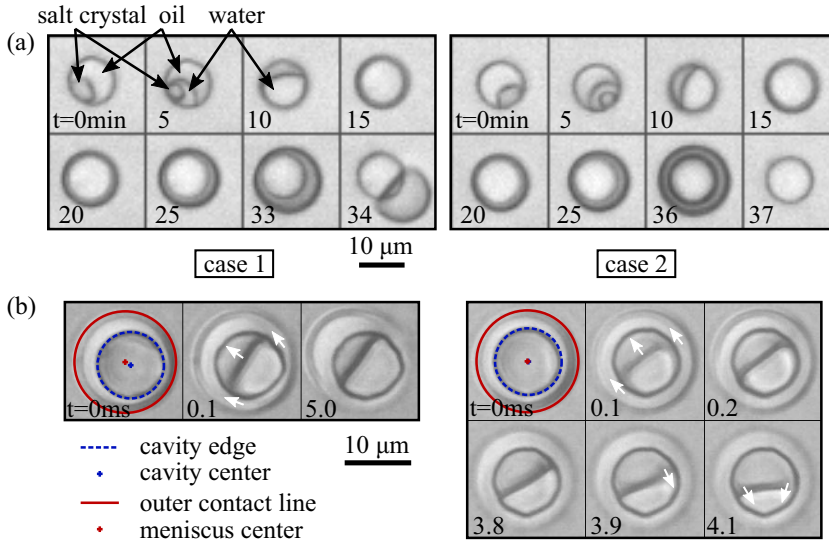


FIG. 6. (a) Oil (hexadecane) initially trapped in a hydrophobic cylindrical cavity ($r_c = 10 \mu\text{m}$ and $h_c = 7.5 \mu\text{m}$) in the presence of salt ($C_s = 200 \text{ g/l}$) and surrounded by water exhibits two different behaviors (cases 1 and 2) as observed from above, where $t = 0$ corresponds to the time when the surrounding low-salinity water is added and (b) with a higher time resolution. Here $t = 0$ corresponds to the time when the oil film bursts. Arrows indicate direction of oil motion.

salted water volume, the inner contact line that separates salted water and oil is moving towards the cavity edge. The bottom wall of the microcavity is fully wet by the HSW after $14.8 \pm 1 \text{ min}$. The outer contact line, initially pinned at the top edge of the cavity, starts to move at $t = 18 \pm 2 \text{ min}$. The salted water pocket swells under osmosis and thus blows the oil meniscus as a spherical film attached to the solid wall, like a soap bubble [Fig. 7(a)]. Then the inner water phase connects the surrounding water phase via a rupture of the oil film at $t = 30 \pm 5 \text{ min}$, as sketched in Figs. 7(b) and 7(c). Two outcomes are observed: Either the oil forms an oil drop close to the cavity [Fig. 6(a),

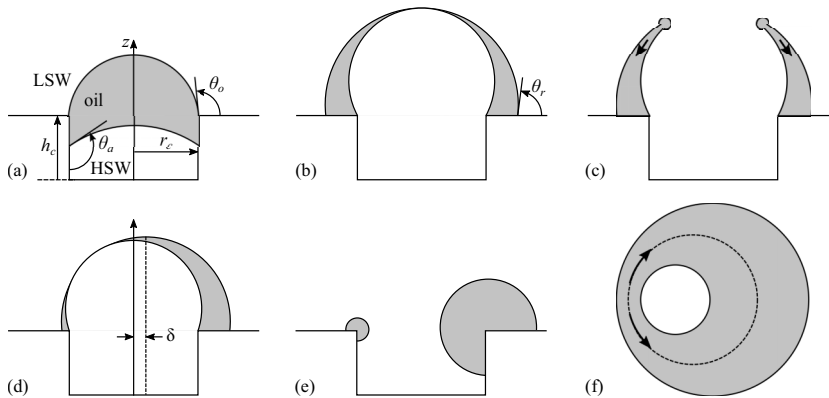


FIG. 7. (a) Schematics of the side view of an oil meniscus moving in a hydrophobic cavity, (b) prior to the oil film rupture and (c) right after. Also shown are the schematics of an asymmetric oil meniscus (d) before bursting and (e) after oil recoiling at the cavity edge, as well as (f) a representation from above. The dotted circle underlines the cavity edge and arrows indicate liquid motion.

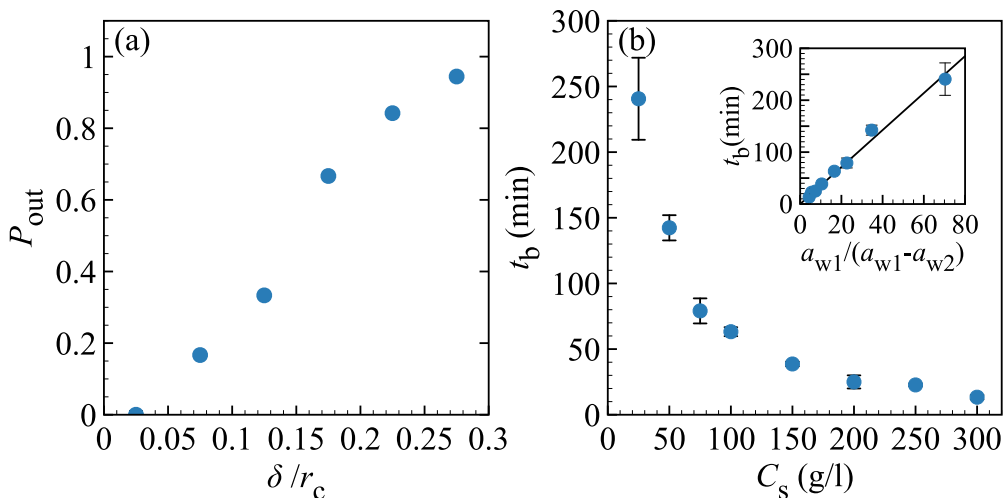


FIG. 8. (a) Probability P_{out} of oil to escape from a hydrophobic cavity as a function of the relative off-centered distance δ/r_c that characterizes the asymmetry feature of the oil meniscus. (b) Bursting time t_b of oil menisci as a function of the salt concentration C_s initially filling the microcavities. The inset shows the bursting time as a function of the inverse of the relative water activity mismatch.

case 1] or the oil moves back inside the cavity [Fig. 6(a), case 2]. This is supported by high-speed recordings that allow us to visualize the motion of the oil-water interface just after the rupture of the oil film [Fig. 6(b)]. For case 1, we note that the oil meniscus center does not match with the cavity center. This mismatch is illustrated by the snapshot taken prior to the burst of the oil film at $t = 33$ min in Fig. 6(a). The off-center distance δ results from an anisotropic spreading of the oil [Fig. 7(d)]. The oil film ruptures by the nucleation of a hole, most probably in the thinnest part of the film, therefore where the outer contact line is closer to the cavity edge. The recoiling of the suspended oil film driven by interfacial tension leads to the formation of an asymmetric ring of oil sitting at the top cavity edge [Fig. 7(e)]. This asymmetry introduces a variation of surface curvature and thus a gradient of capillary pressure that favors draining of the oil towards the forming drop [Fig. 7(f)].

For case 2, the oil meniscus and the cavity are almost centered as observed in Fig. 6(a) at $t = 36$ min. There is still an asymmetry after bursting (the rupture did not occur at the apex); however, the forming oil drop is not enough out of the cavity to prevent its surface from contacting the cavity bottom wall. In that case, a spreading of the oil back into the microcavity is observed. Because of heterogeneities of the surface properties, as revealed by contact angle hysteresis, the off-center distance δ varies from one cavity to another. In addition, there exists a probability P_{out} for oil to escape that depends on δ ; P_{out} is higher than 0.5 if the δ/r_c is higher than 0.15 and almost equal to 1 for $\delta/r_c = 0.3$ [Fig. 8(a)]. Wetting heterogeneities therefore favor efficient oil escape from a hydrophobic cavity through this osmosis mechanism.

As previously discussed, water diffuses through the oil meniscus to balance its chemical potential linked to ion concentration in each aqueous reservoir. The flux of water molecules, and thus the swelling dynamics of the salted water pocket that leads to the oil meniscus bursting, is governed by this salt concentration mismatch. Indeed, the bursting time is a decreasing function of the concentration C_s of the HSW initially trapped in the microcavities [Fig. 8(b)]. The flux of water molecules J_w through an oil slab of thickness h sandwiched between two aqueous reservoirs having water activities a_{w1} and a_{w2} , respectively, is given by Eq. (8). The bursting time t_b is inversely proportional to the time integral of the flux J_w . If one assumes a constant oil thickness, and thus a constant water flux, then $t_b \sim a_{w1}/(a_{w1} - a_{w2})$. This rough estimate, where time variation of the

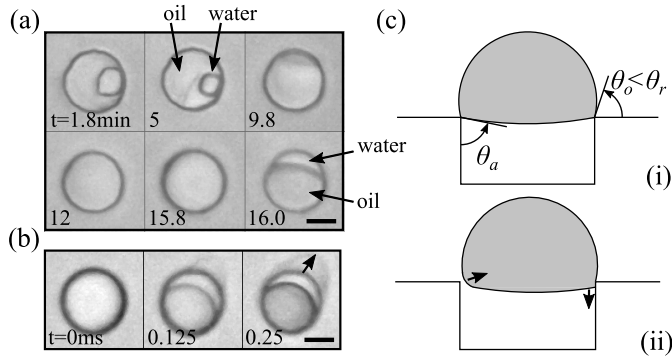


FIG. 9. (a) Dynamics of an oil meniscus in a hydrophilic microcavity with the same conditions as in Fig. 6 ($h_c/r_c = 0.75$). Surface modification is made by exposing the substrate to oxygen plasma for 12 s. (b) High-speed imaging when the meniscus bursts. The arrow indicates the ejection of the salted water. (c) Schematics of the side view of the oil meniscus moving in a hydrophilic cavity (i) prior to the oil meniscus rupture at the triple line location and (ii) after. Scale bars are $5 \mu\text{m}$ and arrows indicate interface motion.

meniscus geometry and the water activity are not taken into account, is in good accordance with experimental data [Fig. 8(b) inset].

2. Hydrophilic microcavity

When the solid wall is made hydrophilic, we observe a different dynamics, as exemplified in Fig. 9. Similar microcavities reported in Fig. 6(b) are here exposed to oxygen plasma for 12 s. While the time needed to dissolve the salt crystal is similar, 7.5 ± 0.5 min, water fully wets the bottom wall in a shorter time, 8.9 ± 0.5 min. Then the salted water pocket is connected to the surrounding phase at $t = 14.3 \pm 0.5$ min. High-speed imaging reveals the fast expulsion of the salted water induced by the motion of the oil-water interface driven by surface tension. In that case, the oil never escapes from the cavity and finally rests on the side of the cavity. Knowing the values of contact angles, the meniscus shape can be reconstructed as shown in Fig. 9(c). The inner contact angle corresponds to the advancing one θ_a , while the outer one, if the contact line does not move away from the edge, is smaller than the receding one θ_r . In that case, the two triple lines meet at the cavity edge. A hole that induces dewetting is nucleated at the meniscus foot which promotes a spreading of oil back inside the cavity. It is thus impossible to remove oil from this hydrophilic cavity.

3. Microcavity with a high aspect ratio

We could not manage to fabricate too-high-aspect-ratio crevices, but for a larger aspect ratio equal to 2.6, we observe an interesting phenomenon as reported in Fig. 10 for hydrophobic microcavities. The outer contact line moves farther away from the cavity because of a larger amount

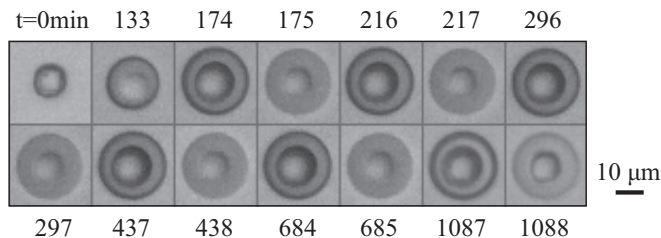


FIG. 10. Bubbling meniscus in a hydrophobic cavity with $h_c/r_c = 2.65$ for $C_s = 200$ g/l.

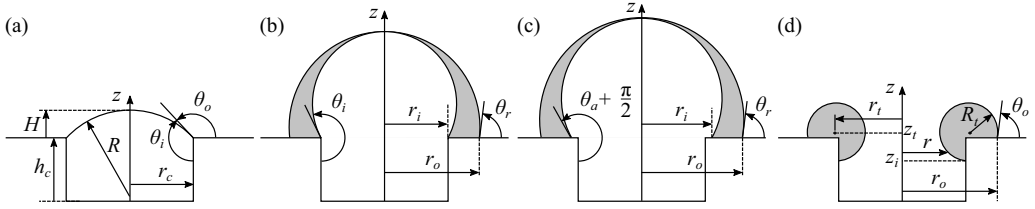


FIG. 11. (a) Schematics of a truncated sphere at the cavity edge. (b) Schematics of the side view of an oil meniscus moving out from a hydrophobic cavity when the inner contact line is pinned at the cavity edge prior to bursting and (c) when the inner contact line moves on the outer wall prior to bursting. (d) Schematics of an oil torus sitting at the cavity's edge after the burst of the oil film.

of trapped oil. Then the oil film bursts after 175 min, but the salted water pocket swells again, leading to another oil film rupture at $t = 217$ min. The phenomenon of perforation and healing of the oil film is repeated with a time period between two connections of the water reservoirs that increases with time, concomitant with a dilution of the HSW reservoir. We note that all the microcavities on the same substrate exhibit the same behavior of bubbling, whatever the heterogeneities of wetting properties. Increasing the aspect ratio of the oil trap is therefore beneficial for oil removal.

C. Features of the oil torus at the cavity's edge

After the connection of the two aqueous reservoirs, the oil is pulled back at the microcavity edge. As discussed above, the final location of the oil depends on wetting properties and microcavity aspect ratio. These observations are now rationalized by geometrical arguments.

1. Condition for creating a torus

Let us first determine the critical aspect ratio of the cavity $(h_c/r_c)^*$ below which the two water reservoirs are connected at the cavity edge when the two triple lines meet and thus above which a liquid torus can be formed. The outer contact line starts to move away from the edge as soon as the outer contact line θ_o is equal to the receding one [Figs. 7(a) and 7(b)]. The critical aspect ratio is thus set at $\theta_o = \theta_r$. Since the inner contact line is moving up to the edge, the inner contact angle θ_i is thus equal to θ_a . A first condition is that $\theta_a \geq \theta_r$. A second condition is that the volume between the two liquid-liquid interfaces is equal to the initial volume of oil V_{oil} trapped in the cavity. The initial conditions are such that the area between the oil and the low-salinity water reservoir is minimal. Since the outer contact line is localized at a right angle edge, the contact angle can vary up to $\pi/2$. Considering the value of the advancing and receding contact angles, we can assume that the interface is flat. The volume of oil V_{oil} trapped in the cavity is thus simply $\pi r_c^2 h_c$. Then, for a given set of advancing and receding contact angles, one has to determine the volume of oil such that the two triple lines are located at the cavity edge. Since gravity does not play a role here, the maximal Bond number $Bo = \Delta\rho g r_c^2 / \gamma$ is 2×10^{-10} and the curvature of the liquid-liquid interfaces is constant. Therefore, one has to evaluate volumes of truncated spheres defined by the two liquid-liquid interfaces [Fig. 11(a)]. The volume of a spherical cap is

$$V_{cap} = \frac{\pi}{3} H^2 (3r - H), \quad (13)$$

where R is the sphere radius, r the radius of the base of the cap, and H the height of the cap. The cap volume can then be expressed as a function of r , which corresponds here to the cavity radius r_c , and the angle that makes the cap with the vertical or horizontal at its base, which corresponds to either the inner or the outer contact angle. For the example shown in Fig. 11(a), since $H = R - (R^2 - r_c^2)^{1/2}$

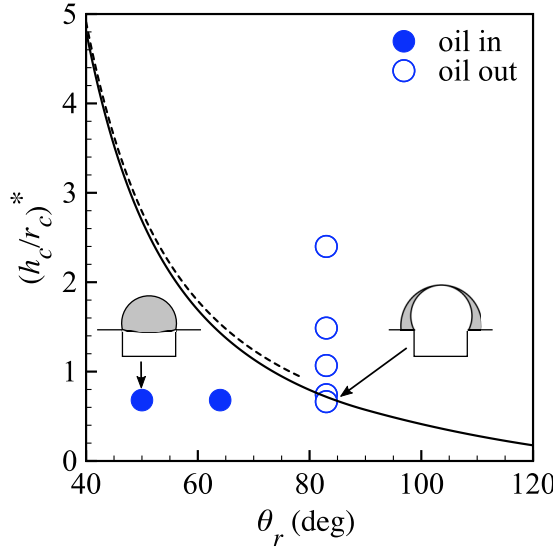


FIG. 12. Critical aspect ratio of the microcavity below which the two contact lines meet at the cavity edge as a function of the receding contact angle for $\theta_a = 126^\circ$ (solid line) and $\theta_a = 80^\circ$ (dashed line). The symbols represent experiments where oil does not move out (\bullet) for $\theta_a < 80^\circ$, i.e., for hydrophilic cavities, and where oil can move out (\circ) for $\theta_a = 126^\circ$, i.e., for hydrophobic cavities.

and $R = -r_c \sec \theta_i = r_c \csc \theta_o$, the cap volume is

$$V_{\text{cap}} = \frac{\pi}{3} r_c^3 f(\theta_i) = \frac{\pi}{3} r_c^3 f(\theta_o + \pi/2), \quad (14)$$

where

$$f(\theta) = (|\sec \theta| - |\tan \theta|)^2 (3 - |\sec \theta| + |\tan \theta|). \quad (15)$$

The evaluation of the critical aspect ratio of the cavity below which the two aqueous reservoirs are connected via the two triple lines depends on the value of the contact angles since then $\theta_i = \theta_a$ and $\theta_o = \theta_r$. If $\theta_r \geq \pi/2$ one gets

$$\left(\frac{h_c}{r_c}\right)^* = \frac{1}{3} [f(\theta_r + \pi/2) - f(\theta_a)]. \quad (16)$$

If $\theta_r \leq \pi/2$ and $\theta_a \leq \pi/2$, the critical ratio is

$$\left(\frac{h_c}{r_c}\right)^* = \frac{1}{3} [4 \csc^3 \theta_r - f(\theta_r + \pi/2) + f(\theta_a)]. \quad (17)$$

If $\theta_r \leq \pi/2$ and $\theta_a \geq \pi/2$, the critical ratio is

$$\left(\frac{h_c}{r_c}\right)^* = \frac{1}{3} [4 \csc^3 \theta_r - f(\theta_r + \pi/2) - f(\theta_a)]. \quad (18)$$

The critical aspect ratio is plotted in Fig. 12 as a function of the receding contact angle for two different advancing contact angles corresponding to experimental conditions. While $(h_c/r_c)^*$ decreases rapidly when θ_r increases, it is a weak function of θ_a . For the present experiments with bare surfaces of NOA81, the critical aspect ratio given by Eq. (18) is equal to 0.72 ± 0.06 . For a substrate exposed to oxygen plasma, the critical aspect ratio given by Eq. (17) is equal to 1.4 ± 0.2 and 2.8 ± 0.3 for exposure times of 6 and 12 s, respectively. To compare with experiments,

one has to subtract from V_{oil} the volume of salt $V_s = C_s \pi r_c^2 h_c / \rho_s$ initially solubilized in the high-salinity water phase, where ρ_s is the salt density, C_s is the salt concentration, and the volume of the trapped water is also assumed to be equal to the cavity volume. We can then consider an equivalent cavity depth $h_{c,eq} = h_c(1 - C_s/\rho_s)$. As shown in Fig. 12, the experimental observations are in good agreement with this geometrical analysis.

The outer contact line starts to move away from the cavity's edge once the aspect ratio of the cavity is larger than $(h_c/r_c)^*$. In that case, the two aqueous phases are connected at the apex of the liquid-liquid interfaces [Fig. 10(b)]. The location r_o of the outer contact line and the contact angle then set the features of the truncated liquid torus [Fig. 10(d)], i.e., the tube's radius r_t and the distance from the center of the torus to the center of the tube R_t . Indeed, we experimentally observe that the outer contact line is initially pinned after the oil meniscus bursts. The derivation of r_o as a function of the aspect ratio and the wetting conditions is given in the Appendix.

2. Torus features

The oil meniscus is blown up by osmotic pressure while being attached to the solid surface outside the cavity, like a soap bubble. While the location and mechanism of perforation in free film are still debated [30,31], we assume here that the oil film ruptures at the apex where the film thickness is minimal. The hole connecting the two water reservoirs then expands due to the interfacial tension and the oil is collected in a rim that surrounds the hole [32]. The outer contact line is pinned at r_o at an angle θ_o and the inner one moves back inside the cavity down to $z = z_i$. The oil is finally shaped as a truncated torus at the cavity edge whose center is at a radius r_t and characterized by a cylinder radius R_t [Fig. 10(d)]. The truncated volume V_{tr} is

$$V_{tr} = \pi \int_{z_i}^{h_c} \{r_t + [R_t^2 - (z - z_t)^2]^{1/2}\}^2 dz - \pi r_c^2 (h_c - z_i), \quad (19)$$

where

$$z_c = h_c + R_t \cos \theta_o, \quad (20)$$

$$z_i = z_c - R_t \sin \theta_o, \quad (21)$$

$$r_t = r_o - R_t \sin \theta_o. \quad (22)$$

Conservation of the oil volume leads to the equation

$$2\pi^2 r_t R_t^2 - V_{tr} = \pi r_c^2 h_c. \quad (23)$$

There are two unknowns parameters r_t and R_t . We assume here that the outer contact angle θ_o corresponds to the receding one prior to the oil film burst, i.e., $\theta_o = \theta_r$. The geometrical features of the truncated torus can then be determined by solving numerically Eq. (23).

Returning to the bubbling behavior shown in Fig. 10, the healing process resembles the shrinking of a liquid torus as previously reported [33]. Indeed, the capillary pressure is always larger on the exterior side of the torus than on the interior, a situation that can induce a closure of the interior hole of the torus before Rayleigh-Plateau instability takes place [34]. Torus shrinking, i.e., for an axisymmetric collapse of the torus, and thus bubbling, occurs for $r_t/2R_t < 1$. As previously discussed, we make here the assumption that the oil film recoils as a truncated torus sitting on the cavity's edge after the oil film ruptures at the apex of the meniscus [Fig. 11(d)]. The geometrical properties of the torus, namely, r_t and R_t , depend on the location r_o of the outer contact line, which is a function of the aspect ratio of the microcavities and the dynamic contact angles. Considering the wetting properties of the bare NOA81, r_o is given by Eq. (A2) and by Eq. (A19) when $h_c/r_c > 1.95$. Then r_t is linked to R_t through Eq. (22), which is found by solving Eq. (23). Including variation of the contact angles (Table I), the ratio $r_t/2R_t$ is plotted as a function of the cavity aspect ratio in Fig. 13. The slope of the curve rapidly changes when the inner contact line moves away from

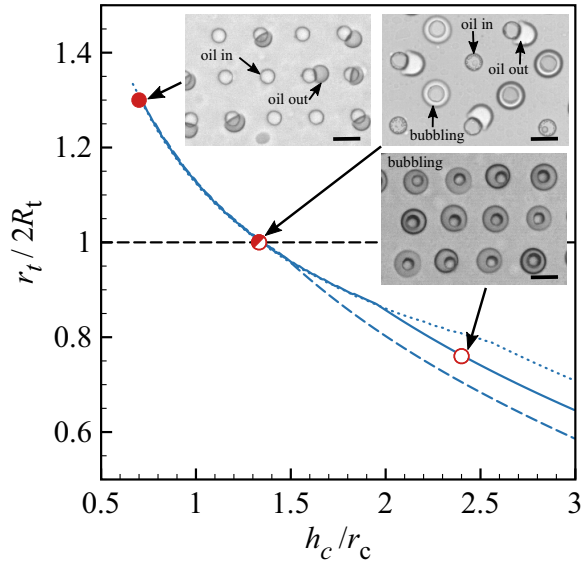


FIG. 13. Aspect ratio $r_t/2R_t$ of the equivalent oil torus after meniscus burst as a function of the cavity aspect ratio predicted with the average contact angles (solid line), the maximal ones (dotted line), and the minimal ones (dashed line) for a bare substrate. Bubbling occurs when the torus shrinks for $r_t/2R_t < 1$ and thus closes the hole that connects the two aqueous reservoirs. Pictures represent different values of $h_{c,eq}/r_c$ after menisci bursting.

the cavity, i.e., when $\theta_i > \theta_a + \pi/2$. The transition between the two regimes, a longitudinal flow of oil in the liquid torus that leads to either a drop of oil outside or inside the cavity ($r_t/2R_t > 1$) or a radial flow that induces torus shrinking and thus a bubbling phenomenon ($r_t/2R_t < 1$), is well accounted for. Indeed, we note that the microcavities for which $h_{c,eq}/r_c = 1.3$ sits at the frontier between radial and longitudinal collapse of the torus exhibit these three behaviors.

IV. CONCLUSION AND PERSPECTIVES

In this article, two experimental setups were used to establish the dynamics and the mechanisms of oil removal from a porous system by osmosis and their links to wetting properties. The first system, where oil is sandwiched between two salted aqueous reservoirs in a glass capillary, allowed us to assess the water permeability features of the oil by monitoring oil displacement as a consequence of water diffusion. Here wetting properties of the different phases on the solid wall rule the shape of the oil meniscus and thus alter the water flux. The permeability, governed by the coefficient of diffusion of water molecules and the solubility of water in oil, was assessed for a pure hydrocarbon oil as well as for crude oil. Given the value of crude oil viscosity and water solubility, an enhanced flux of water was measured. Moreover, the addition of asphaltenes in a pure hydrocarbon oil was shown to enhance water transport between the two aqueous phases, while the water solubility was barely modified. We also noted the nucleation of water droplets at the oil-LSW interface. Further investigations would provide additional insight into the increase of water transport and its potential link with spontaneous emulsification in the presence of surface active compounds.

The second system elaborated consists of microcavities mimicking dead-end pores where oil is trapped in the presence of salt crystal. The efficiency of osmosis for moving out oil from a microcavity is intrinsically linked to wetting properties, including heterogeneities of surface properties. Counterintuitively, removing oil from a hydrophilic cavity is less probable than from a hydrophobic one. In real systems, such as porous materials, an isolated oil pocket is a peculiar

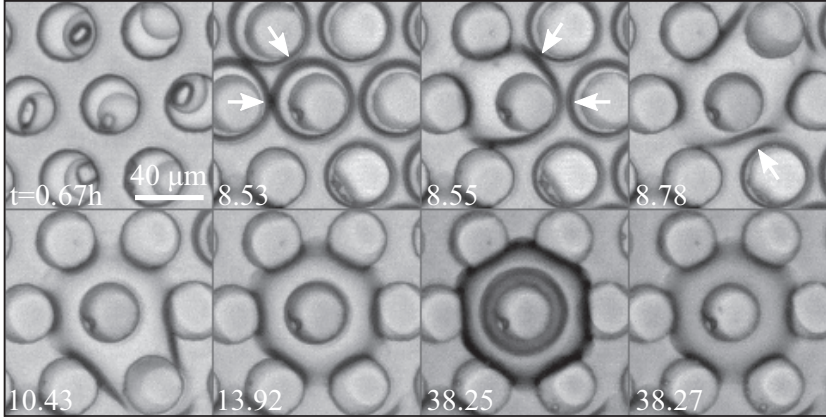


FIG. 14. Interaction of oil menisci from hydrophobic microcavities with $h_c/r_c = 1.5$, i.e., $h_{c,eq}/r_c = 1.3$ for $C_s = 200$ g/l, leading to coalescence of adjacent oil pockets indicated by arrows. The merged drops then exhibit a bubbling behavior.

case. When the outer contact line location overlaps with about half of the minimal distance between the edges of two cavities, neighboring menisci may indeed interact. As reported in Fig. 14, adjacent oil menisci coalesce. Merging induces lateral motion of the oil and thus a local increase of oil volume over a cavity where bubbling, thus efficient oil removal, is observed. How geometry, i.e., aspect ratio and spatial distribution of microcavities, modifies oil removal efficiency is a question left for future work.

ACKNOWLEDGMENTS

This work received support from Total SA and Institut Pierre-Gilles de Gennes (équipement d'excellence, "Investissements d'avenir" Program No. ANR-10-EQPX-34).

APPENDIX

The location r_o of the outer contact line is here determined as a function of the aspect ratio and the wetting conditions.

1. Meniscus features when the inner contact line is pinned at the cavity edge

Let us first determine the location r_o of the outer contact line when the inner contact line is pinned at the cavity edge [Fig. 10(b)]. It follows that $r_i = r_c$, $\theta_o = \theta_r$ and $\theta_i \in [\theta_a, \theta_a + \pi/2]$.

Case 1. If $\theta_r \geq \pi/2$ and $\pi/2 \leq \theta_i \leq \pi$, the two interfaces connect at their apexes when

$$H_i = H_o. \quad (\text{A1})$$

This leads to a relationship between the locations of the two contact lines

$$r_o = \alpha_1(\theta_i, \theta_r)r_c, \quad (\text{A2})$$

where

$$\alpha_1(\theta_1, \theta_2) = \frac{-\sec \theta_1 - |\tan \theta_1|}{\csc \theta_2 - |\cot \theta_2|}. \quad (\text{A3})$$

Using volume conservation, the inner contact angle is a solution of the equation

$$\alpha_1^3(\theta_i, \theta_r)f(\theta_r + \pi/2) - f(\theta_i) = 3\frac{h_c}{r_c}. \quad (\text{A4})$$

The inner contact line starts to move away from the cavity's edge once the aspect ratio of the cavity is larger than $(h_c/r_c)^{**}$ for $\theta_i = \theta_a + \pi/2$. We finally obtain

$$\left(\frac{h_c}{r_c}\right)^{**} = \frac{1}{3}[\alpha_1^3(\theta_a + \pi/2, \theta_r)f(\theta_r + \pi/2) - f(\theta_a + \pi/2)]. \quad (\text{A5})$$

Case 2. If $\theta_r \geq \pi/2$ and/or $\pi \leq \theta_i \leq 3\pi/2$, the two interfaces connect at the apex when

$$2R_i - H_i = H_o. \quad (\text{A6})$$

In that case

$$r_o = \alpha_2(\theta_i, \theta_r)r_c, \quad (\text{A7})$$

where

$$\alpha_2(\theta_1, \theta_2) = \frac{-\sec \theta_1 + |\tan \theta_1|}{\csc \theta_2 - |\cot \theta_2|}. \quad (\text{A8})$$

Volume conservation leads to the following equation for θ_i :

$$\alpha_2^3(\theta_i, \theta_r)f(\theta_r + \pi/2) + 4 \sec^3 \theta_i + f(\theta_i) = 3\frac{h_c}{r_c}. \quad (\text{A9})$$

The critical aspect ratio is then

$$\left(\frac{h_c}{r_c}\right)^{**} = \frac{1}{3}[\alpha_2^3(\theta_a + \pi/2, \theta_r)f(\theta_r + \pi/2) + 4 \sec^3(\theta_i + \pi/2) + f(\theta_a + \pi/2)]. \quad (\text{A10})$$

Case 3. If $\theta_r \leq \pi/2$, the interfaces meet at their apexes if $\theta_i \geq \pi$ and thus when

$$2R_i - H_i = 2R_o - H_o. \quad (\text{A11})$$

In that case

$$r_o = \alpha_3(\theta_i, \theta_r)r_c, \quad (\text{A12})$$

where

$$\alpha_3(\theta_1, \theta_2) = \frac{-\sec \theta_1 + |\tan \theta_1|}{\csc \theta_2 + |\cot \theta_2|}. \quad (\text{A13})$$

Volume conservation leads to the following equation for θ_i :

$$\alpha_3^3(\theta_i, \theta_r)[4 \csc^3 \theta_r - f(\theta_r + \pi/2)] + 4 \sec^3 \theta_i + f(\theta_i) = 3\frac{h_c}{r_c}. \quad (\text{A14})$$

The critical aspect ratio is then

$$\left(\frac{h_c}{r_c}\right)^{**} = \frac{1}{3}\{\alpha_3^3(\theta_a + \pi/2, \theta_r)[4 \csc^3 \theta_r - f(\theta_r + \pi/2)] + 4 \sec^3(\theta_i + \pi/2) + f(\theta_a + \pi/2)\}. \quad (\text{A15})$$

For the present experiments with bare surfaces of NOA81, the critical aspect ratio given by Eq. (A15) is equal to 1.95, thus below the one used in the experiments shown in Fig. 10.

2. Meniscus feature when the inner contact line moves away from the cavity edge

Now the inner contact line is also away from the cavity edge [Fig. 10(c)], i.e., $r_i > r_c$, and thus $\theta_i = \theta_a + \pi/2$.

Case 1. If $\theta_r \geq \pi/2$, since $\theta_a \geq \theta_r$ the two aqueous reservoirs are connected when

$$2R_i - H_i = H_o \quad (\text{A16})$$

and

$$r_o = \alpha_2(\theta_a + \pi/2, \theta_r) \left(\frac{3r_c^2 h_c}{\alpha_2^3(\theta_a + \pi/2, \theta_r) f(\theta_r + \pi/2) - 4 \csc^3 \theta_a + f(\theta_a + \pi/2)} \right)^{1/3}. \quad (\text{A17})$$

Case 2. If $\theta_r \leq \pi/2$, connection is made when

$$2R_i - H_i = 2R_o - H_o \quad (\text{A18})$$

and thus

$$r_o = \alpha_3(\theta_a + \pi/2, \theta_r) \left(\frac{3r_c^2 h_c}{\alpha_3^3(\theta_a + \pi/2, \theta_r) [4 \csc^3 \theta_r - f(\theta_r + \pi/2)] - 4 \csc^3 \theta_a + f(\theta_a + \pi/2)} \right)^{1/3}. \quad (\text{A19})$$

-
- [1] J. N. Israelachvili, *Intermolecular and Surface Forces* (Academic, New York, 1991).
- [2] P.-G. de Gennes, F. Brochard-Wyart, and D. Quéré, *Capillarity and Wetting Phenomena: Drops, Bubbles, Pearls, Waves* (Springer, New York, 2004).
- [3] N. Morrow and J. Buckley, Improved oil recovery by low-salinity waterflooding, *J. Petrol. Technol.* **63**, 106 (2011).
- [4] J. J. Sheng, Critical review of low-salinity waterflooding, *J. Petrol. Sci. Eng.* **120**, 216 (2014).
- [5] F. Mugele, B. Bera, A. Cavalli, I. Siretanu, A. Maestro, M. Duits, M. Cohen-Stuart, D. van den Ende, I. Stocker, and I. Collins, Ion adsorption-induced wetting transition in oil-water-mineral systems, *Sci. Rep.* **5**, 10519 (2015).
- [6] S.-Y. Chen, K. Kristiansen, D. Seo, N. A. Cadirov, H. A. Dobbs, Y. Kaufman, A. M. Schrader, R. C. Andresen Eguluz, M. B. Alotaibi, S. C. Ayirala *et al.*, Time-dependent physicochemical changes of carbonate surfaces from smartwater (diluted seawater) flooding processes for improved oil recovery, *Langmuir* **35**, 41 (2019).
- [7] K. Sandengen, A. Kristoffersen, K. Melhuus, and L. O. Jøsang, Osmosis as mechanism for low-salinity enhanced oil recovery, *SPE J.* **21**, 1227 (2016).
- [8] S. B. Fredriksen, A. U. Rognmo, K. Sandengen, and M. A. Fernø, Wettability effects on osmosis as an oil-mobilization mechanism during low-salinity waterflooding, *Petrophysics* **58**, 28 (2017).
- [9] L. Yan, H. Aslannejad, S. M. Hassanizadeh, and A. Raouf, Impact of water salinity differential on a crude oil droplet constrained in a capillary: Pore-scale mechanisms, *Fuel* **274**, 117798 (2020).
- [10] A. Kabalnov, Ostwald ripening and related phenomena, *J. Disper. Sci. Technol.* **22**, 1 (2001).
- [11] A. Saint-Jalmes, Physical chemistry in foam drainage and coarsening, *Soft Matter* **2**, 836 (2006).
- [12] L. Boitard, D. Cottinet, C. Kleinschmitt, N. Bremond, J. Baudry, G. Yvert, and J. Bibette, Monitoring single-cell bioenergetics via the coarsening of emulsion droplets, *Proc. Natl. Acad. Sci. USA* **109**, 7181 (2012).
- [13] A. R. Thiam, N. Bremond, and J. Bibette, From stability to permeability of adhesive emulsion bilayers, *Langmuir* **28**, 6291 (2012).
- [14] G. Villar, A. D. Graham, and H. Bayley, A tissue-like printed material, *Science* **340**, 48 (2013).
- [15] P. Gruner, B. Riechers, B. Semin, J. Lim, A. Johnston, K. Short, and J.-C. Baret, Controlling molecular transport in minimal emulsions, *Nat. Commun.* **7**, 10392 (2016).

- [16] Z. Hua, M. Li, X. Ni, H. Wang, Z. Yang, and M. Lin, Effect of injection brine composition on wettability and oil recovery in sandstone reservoirs, *Fuel* **182**, 687 (2016).
- [17] S. B. Fredriksen, A. U. Rognmo, and M. A. Fernø, Pore-scale mechanisms during low salinity waterflooding: Oil mobilization by diffusion and osmosis, *J. Petrol. Sci. Eng.* **163**, 650 (2018).
- [18] D. Bartolo, G. Degre, P. Nghe, and V. Studer, Microfluidic stickers, *Lab Chip* **8**, 274 (2008).
- [19] Y. Xia and G. M. Whitesides, Soft lithography, *Annu. Rev. Mater. Sci.* **28**, 153 (1998).
- [20] N. Bremond, M. Arora, C. D. Ohl, and D. Lohse, Controlled Multibubble Surface Cavitation, *Phys. Rev. Lett.* **96**, 224501 (2006).
- [21] B. J. Zwolinski, H. Eyring, and C. E. Reese, Diffusion and membrane permeability, *J. Phys. Chem.* **53**, 1426 (1949).
- [22] W. J. Hamer and Y. Wu, Osmotic coefficients and mean activity coefficients of uni-univalent electrolytes in water at 25 °C, *J. Phys. Chem. Ref. Data* **1**, 1047 (1972).
- [23] C. Tsonopoulos, Thermodynamic analysis of the mutual solubilities of normal alkanes and water, *Fluid Phase Equilib.* **156**, 21 (1999).
- [24] J. T. Su, P. B. Duncan, A. Momaya, A. Jutila, and D. Needham, The effect of hydrogen bonding on the diffusion of water in *n*-alkanes and *n*-alcohols measured with a novel single microdroplet method, *J. Chem. Phys.* **132**, 044506 (2010).
- [25] T. Klein, S. Yan, J. Cui, J. W. Magee, K. Kroenlein, M. H. Rausch, T. M. Koller, and A. P. Fröba, Liquid viscosity and surface tension of *n*-hexane, *n*-octane, *n*-decane, and *n*-hexadecane up to 573 K by surface light scattering, *J. Chem. Eng. Data* **64**, 4116 (2019).
- [26] D. Langevin and J.-F. Argillier, Interfacial behavior of asphaltenes, *Adv. Colloid. Interface Sci.* **233**, 83 (2016).
- [27] F. P. Lees and P. Sarram, Diffusion coefficient of water in some organic liquids, *J. Chem. Eng. Data* **16**, 41 (1971).
- [28] S. I. Andersen, J. M. del Rio, D. Khvostitchenko, S. Shakir, and C. Lira-Galeana, Interaction and solubilization of water by petroleum asphaltenes in organic solution, *Langmuir* **17**, 307 (2001).
- [29] S. Bochner de Araujo, M. Merola, D. Vlassopoulos, and G. G. Fuller, Droplet coalescence and spontaneous emulsification in the presence of asphaltene adsorption, *Langmuir* **33**, 10501 (2017).
- [30] S. Poulain, E. Villermaux, and L. Bourouiba, Ageing and burst of surface bubbles, *J. Fluid Mech.* **851**, 636 (2018).
- [31] B. Néel and E. Villermaux, The spontaneous puncture of thick liquid films, *J. Fluid Mech.* **838**, 192 (2018).
- [32] G. I. Taylor, The dynamics of thin sheets of fluid. III. disintegration of fluid sheets, *Proc. R. Soc. London Ser. A* **253**, 313 (1959).
- [33] E. Páram and A. Fernandez-Nieves, Generation and Stability of Toroidal Droplets in a Viscous Liquid, *Phys. Rev. Lett.* **102**, 234501 (2009).
- [34] Z. Yao and M. J. Bowick, The shrinking instability of toroidal liquid droplets in the Stokes flow regime, *Eur. Phys. J. E* **34**, 32 (2011).